Highly efficient La/Ni co-doped strontium titanate catalyst for co-production of propylene and hydrogen from propane in protonic ceramic electrochemical cells

Yuqing Meng [a,1], Hao Deng [b,1], Lu-Cun Wang [a,*], Daekun Kim [c], Bin Liu [b], Fudong Liu [c], Yong Ding [d], Dong Ding [a,*]

[a] Energy & Environmental Science and Technology, Idaho National Laboratory, Idaho Falls, ID 83401, USA
[b] Tim Taylor Department of Chemical Engineering, Kansas State University, Manhattan, KS 66506, USA
[c] Department of Civil, Environmental, and Construction Engineering, University of Central Florida, Orlando, FL 32816, USA
[d] School of Materials Science and Engineering, Georgia Institute of Technology, Atlanta, GA 30332, USA

ARTICLE INFO

ABSTRACT

A highly efficient La/Ni co-doped strontium titanate (LSNT) perovskite catalyst is developed and integrated in a protonic ceramic electrochemical cell for co-production of propylene and high-purity hydrogen from commercial propane feedstock. Propane conversion and hydrogen production rate can be effectively enhanced under an applied current due to the electrochemical promotion effect and/or shifted reaction equilibrium induced by rapid separation of hydrogen product. Water vapor in the feed gas could significantly improve the catalyst stability by suppressing the coke formation. The propane conversion could reach up to 53% at 600 °C under a current density of 90 mA cm^{-2}. The LSNT catalyst also shows excellent tolerance for the sulfur contaminant in commercial propane gas. The excellent performance of the LSNT catalyst is attributed to the highly active and selective Ni species at the interface with the perovskite substrate, which are formed *in situ* via reduction-induced exsolution under reaction conditions.

1. Introduction

Propylene is one of the most important petrochemical intermediates nowadays, the second largest consumed globally, behind ethylene [4]. As another important fuel/chemical, hydrogen plays an increasingly critical role in decarbonization and green economy. Currently, propylene is produced primarily as a by-product of petroleum refining and ethylene production by steam cracking of hydrocarbon feedstocks, while hydrogen is mainly obtained through natural gas reforming. These processes are known to be both highly energy and carbon intensive [2,55]. Recently, on-purpose propylene production by thermal catalytic propane dehydrogenation (PDH) plays an increasingly important role in closing the global shortage in traditional propylene supplies [4,46,8]. The non-oxidative PDH reaction is usually operated at high temperatures around 550–650 °C and suffers from low single-pass conversion limited by thermodynamic equilibrium as well as rapid coking-induced deactivation of the catalysts [46,8]. In addition, the separation of the

major products, namely, propylene and hydrogen, consumes excessive energy with low process efficiency [2]. Hence, it is desirable to develop new types of highly efficient and stable PDH catalysts as well as an energy efficient process to replace the conventional low temperature separation technology.

In principle, propane dehydrogenation and hydrogen separation can be realized through process intensification in a catalytic membrane reactor [45,63,29], which allows for integrated catalytic transformation in tandem with physical/chemical separation of certain products. In this regard, proton-conducting solid-oxide-based electrochemical cells (p-SOC) or membrane reactor systems represent a promising approach toward this goal [59,29,62,58,25,9]. In the p-SOC, the hydrogen byproduct from the PDH reaction can be effectively separated in the form of protons from the product stream through the proton-conducting electrolyte membranes. Timely removal of hydrogen from the product mixture can effectively shift the reaction equilibrium towards the right direction, thus overcoming the thermodynamic limitation and

increasing the single-pass propane conversion. The hydrogen product separated from the PDH reaction can evolve on the other side of the cell and be collected in high purity, which adds the overall benefit of the process in terms of both energy savings and economic gains.

Compared to the conventional oxygen ion conducting solid oxide electrochemical cells (o-SOC), the p-SOC is typically operated at relatively lower temperatures (below 600 °C) [11,6,60]. While the lower operating temperature is beneficial for the structural stability of the cell components and energy consumption, it could significantly retard the reaction kinetics. Accordingly, it is desirable to develop highly efficient catalysts to offset the loss in the yield of olefin products. There have been significant advances recently in developing highly efficient catalysts for thermal catalytic PDH reaction [44,61]. However, the conventional PDH catalysts used in thermal catalytic processes, such as Pt-alloys or CrO$_x$ supported on highly porous materials (e.g., alumina, zeolite) [46,8], may not be suitable for or compatible with the electrochemical cell system due to the low electronic conductivity. The Ni cermet-based electrodes typically used for fuel cell applications usually suffer from low power densities, severe coke deposition, and complex side reactions on the electrodes, mainly due to the excessive catalytic activity of Ni toward hydrocarbon cracking reactions [53,54]. Recently, Shi et al. [48] have reported a novel Pr and Ni co-doped SrTiO$_3$ perovskite catalyst and achieved stable and efficient cogeneration of electricity and light olefins from propane in a protonic solid oxide fuel cell (p-SOFC). Nevertheless, despite the good operating stability, the propane conversion and propylene selectivity at 600 °C were only ~6% and ~27%, respectively [48]. Perovskite catalysts with various compositions have also been employed in several p-SOFC studies using light alkane as feedstock [28, 30,13,12,24,27]. It should be noted, however, that the proton conductors used in most of the previous studies are essentially mixed oxygen-ion and proton conductors since the operating temperatures were usually between 650 °C and 750 °C [38,23]. It is very likely that the alkane dehydrogenation process in these works was an oxidative reaction rather than proceeded via non-oxidative pathways, thus severely limiting the co-production of hydrogen. Therefore, the PDH reaction temperature needs to be at least below 650 °C to minimize the oxygen ion conduction in the electrolyte.

In this work, we report a highly efficient La and Ni co-doped strontium titanate catalyst for the co-production of propylene and high-purity hydrogen from commercial propane feedstock in an electrocatalytic membrane reactor system based on p-SOC. The structure properties of the catalyst were systematically characterized by various techniques including X-ray diffraction (XRD), high resolution transmission electron microscopy (TEM), X-ray photoelectron spectroscopy (XPS), and *in situ* Infrared spectroscopy (IR), etc. The catalytic performance of the catalyst was evaluated both in a conventional fixed bed flow reactor and on the p-SOC under the electrochemical environment. The effect of various factors, such as water vapor, sulfur contaminant in the feed gas, and applied current density, on the catalytic behaviors of the catalyst has also been investigated. Density function theory (DFT) calculations were also performed to gain mechanistic insights into the nature of active sites and the origin of the excellent performance of this LSNT catalyst. In addition to the new PDH catalyst, this work has also demonstrated an alternative technology for on-purpose propylene production with potentially lowered carbon footprint and higher energy efficiency compared with conventional propylene production technologies.

2. Experimental

2.1. Materials synthesis

The (La$_{0.3}$Sr$_{0.7}$)$_{0.9}$Ni$_{0.1}$Ti$_{0.9}$O$_{3-\delta}$ (LSNT) catalyst with A-site deficiency was synthesized by a citric acid combustion method [48,26,33]. Briefly, an aqueous solution of precursors containing lanthanum nitrate, strontium nitrate, nickel nitrate, titanium(IV) isopropoxide, glycine and citric acid was first prepared with the ratio of metal: glycine: citric acid

= 1: 2: 2. The solution was then heated on a hot plate at 90 °C to evaporate the water solvent and form a gel. Once ignited, the gel underwent a combustion process and yielded a voluminous powder. The as-prepared powders were subsequently calcined at 1000 °C for 2 h to form the LSNT perovskite structure. The LSNT sample was reduced in H$_2$ at 900 °C or 1200 °C to facilitate the exsolution of Ni particles. For comparison, the (Pr$_{0.3}$Sr$_{0.7}$)$_{0.9}$Ni$_{0.1}$Ti$_{0.9}$O$_3$ (PSNT) catalyst with A-site deficiency was also synthesized by the same synthesis procedure except that the lanthanum nitrate was replaced by the praseodymium(III) nitrate precursor.

The anode material (PrBa)$_{0.95}$(Fe$_{0.9}$Mo$_{0.1}$)$_2$O$_{5+\delta}$ (PBFM) was prepared by a sol-gel method with ethylenediaminetetraacetic acid (EDTA)-citrate as the complexing agent [59]. The precursor solution containing a stoichiometric amount of praseodymium(III) nitrate, barium nitrate, iron nitrate, and ammonium molybdate was prepared by dissolving in citrate and EDTA-NH$_3$ aqueous solution.

The powders of proton-conducting doped barium zirconates, including BaZr$_{0.8}$Y$_{0.2}$O$_{3-\delta}$ (BZY20) and BaZr$_{0.1}$Ce$_{0.7}$Y$_{0.1}$Yb$_{0.1}$O$_{3-\delta}$ (BZCYYb), were synthesized by a solid-state reaction method. The stoichiometric amount of precursors, including barium carbonate, zirconium oxide, cerium(IV) oxide, yttrium(III) oxide, and ytterbium(III) oxide, were mixed and ball milled for 24 h in ethanol, followed by drying for 24 h. Next, 120 g of the powder was pressed into pellets (7.5 MPa), which were subsequently calcined at 1450 °C for 5 h to form a pure perovskite phase. The pellets were then crushed, and ball milled for another 24 h.

2.2. Characterization

The morphology and the elemental distribution of the catalyst nanoparticles were characterized by field emission scanning electronic microscopy (SEM JEOL 6700 F) with an accelerating voltage of 10 kV combined with energy dispersive X-ray spectroscopy (EDS) analysis. The microstructure and elemental mapping of the materials were also characterized by the scanning transmission electron microscopy (STEM, Tecnai G2 F30S-TWIN) equipped with EDS. The crystalline structure of the catalysts and electrode materials was examined by the XRD analysis (Rigaku SmartLab) with the 2θ ranging from 20° to 80° at a scanning step of 5° min^{-1}.

Temperature programmed reduction experiments (TPR) were performed to investigate the redox properties of the catalyst materials. Typically, 100 mg of the catalyst sample was first pretreated at 120 °C (ramp rate 10 °C min^{-1}) for 30 min in Ar (50 mL min^{-1}) and then cooled down to room temperature. The reduction was conducted in 10% H$_2$/Ar (20 mL min^{-1}) from room temperature to 800 °C at 10 °C min^{-1}. The MS signals including H$_2$ ($m/z = 2$) and H$_2$O ($m/z = 18$) were recorded using the OmniStar gas analysis system (GSD 320 O1).

XPS characterization was performed on Thermo Scientific ESCALAB 250Xi with a monochromatic Al Ka source (photon energy of 1486.68 eV) operated at 30 keV and X-ray power of 150 W and a hemispherical energy analyzer. The samples were degassed in a preparation chamber (10^{-5} Torr) for 30 min and then introduced into an analysis chamber (3 × 10^{-9} Torr) for XPS measurement. High-resolution core level spectra were measured with the pass energy of 150 eV and analysis of the data was carried out using XPSPEAK41 software. The binding energies (BE) of all elements were referenced to the C 1 s line at 284.6 eV.

In situ diffuse reflectance infrared Fourier transformed spectroscopy (DRIFTS) experiments with CO adsorption on the LSNT catalysts were carried out on a Nicolet iS50 Fourier transform infrared spectrometer (Thermo Fisher Scientific) with a mercury cadmium telluride detector cooled by liquid nitrogen. A Harrick high-temperature reaction chamber was loaded with LSNT sample, which was initially treated under the flow of Ar (20 mL min^{-1}) at 200 °C (ramp rate 10 °C min^{-1}) for 1 h to remove any physiosorbed species on the surface. After a steady background was achieved, the sample was exposed to 2%CO/He

(20 mL min^{-1}) for 0.5 h for CO adsorption on the surface of the sample while collecting the IR data. The *in situ* IR spectra with CO chemisorption were collected at room temperature after reaction at 600 °C for different time period (i.e., 1 h, 10 h).

The conductivity of LSNT was measured by a four-probe method with a digital multimeter [19]. In brief, the LSNT ink was brush-painted onto the Al$_2$O$_3$ plate and then fired at 1000 °C for 2 h. The conductivity of the LSNT layer was measured in reducing atmospheres with pure H$_2$.

2.3. Fabrication of button cells

The electrode-supported button cells (10 mm in diameter) with a configuration of LSNT/PBFM|BZY20|CFL|BCZYYb+NiO were fabricated following *a* standard procedure. The NiO+BZY20 was used as the cathode functional layer (CFL) and BCZYYb+NiO was the cathode supporting layer (CSL). To fabricate the electrode support, NiO and BaCe$_{0.7}$Zr$_{0.1}$Y$_{0.1}$Yb$_{0.1}$O$_{3-\delta}$ (BCZYYb) powders with a weight ratio of 60:40 were first blended in a mixture of ethanol and toluene using a high-energy ball mill (SPEX, 8000 M) for 20 min. Subsequently, plasticizers and binders were added to the mixture and milled for another 20 min to obtain a slurry, followed by degassing and tape casting to make green tapes. After drying overnight, the green tape was punched into small coupons of 5/16 in. in size, which were pre-fired at 950 °C for 2 h to form the cathode supports. A thin layer of BZY was then deposited on the cathode support by a slurry coating process and co-fired at 1400 °C for 4 h. Next, the PBFM ink was screen printed onto the top of the BZY electrolyte and fired at 900 °C for 2 h to form a porous cathode. The active electrode area for all cells is 3.1 cm^2.

2.4. Performance evaluation of catalysts and button cells

The thermal catalytic performances of various catalysts were initially evaluated in a fixed-bed tubular flow reactor at different temperatures. Typically, 100 mg of each sample was packed into the fritted reactor with inactive quartz wool to fix the catalyst bed. A propane containing gas mixture (C$_3$H$_8$/H$_2$/Ar = 5/5/40, total flow rate 50 mL min^{-1}) was fed into the reactor. The gas compositions at the reactor outlet were analyzed using gas chromatography (GC, Shimadzu 2010 plus equipped with TCD and FID detectors) to determine the propane conversion and product selectivity. The selectivity was calculated on a carbon basis, which was derived from the peak area of each major product in the gas mixture. Catalyst stability was evaluated using a commercial grade C$_3$H$_8$ gas containing about 0.1% ethyl mercaptan (CH$_3$-CH$_2$-SH) or with 10% steam in the feed gas.

To evaluate the electrochemical performance, the fabricated button cells were sealed in a home-built reactor using a Ceramabond 552 glass sealant. Silver mesh and platinum wire were used as the current collector and leads, respectively. After assembly, the cell was heated up to 650 °C in air to cure the sealant and then switched to pure hydrogen to reduce the nickel oxide in the cathode. After reduction, the temperature was lowered to 600 °C, and the electrochemical performance was measured and analyzed using a Solartron 1400 & 1470 (AMETEK Inc.) electrochemical working station.

2.5. Computational methods

Vienna Ab Initio Simulation Package (VASP) [21,22] was employed to perform spin-polarized periodic DFT calculations and *ab initio* MD (AIMD) simulations. The projector augmented wave (PAW) pseudopotential [7] and the GGA-PBE functional [42] were used to account for the core electrons and the electron exchange-correlation effects. The reciprocal first Brillouin zone was sampled using a 2 × 2 × 1 mesh *k*-point mesh automatically generated from the Monkhorst-Pack scheme [37]. The plane-wave basis set was expanded with a cutoff energy of 400 eV. The electron occupancies were determined using Gaussian smearing (LSNT model, σ = 0.05 eV) and the 1st-order

Methfessel-Paxton scheme (LSNT-Ni$_9$, Ni(211), and Ni(111) models, σ = 0.2 eV) [34]. The structures and energies of all transition states were obtained from the climbing image-nudged elastic band (CI-NEB) method [17] and the dimer method [16].

The following procedure was employed to build the structure of the *in situ* exsolved Ni nanoparticle on LSNT surface. As illustrated in Fig. S7, the bulk LSNT structure was initially built by uniformly and stoichiometrically distributing A and B site elements (8 La, 19 Sr, 3 Ni, 24 Ti, and 81 O), which provided more various atomic environments. To obtain a more realistic configuration, AIMD simulations were performed on LSNT surface with 9 ordered Ni adatoms (144 atoms in total), as shown in Fig. S8A. AIMD simulations were performed with Nosé–Hoover (NVT) thermostat under 800 °C for a simulation time of 3.84 ns (a wall time of 10 days by using 32 cores). After the simulation, as shown in Fig. S8B, the Ni$_9$ cluster became disordered and notable triple junctions responsible for stabilizing the cluster on the surface were formed. Finally, to obtain the stable LSNT-Ni$_9$ model for further DFT calculation, the last frame of AIMD was optimized using DFT calculation, as shown in Fig. S8C.

In addition to the LSNT-Ni$_9$ model, three different models, including LSNT, Ni (211), and Ni (111), were also built as benchmarks for comparison with LSNT-Ni$_9$. Both LSNT-Ni$_9$ and LSNT contain 4 layers of bulk LSNT, with the bottom 2 layers frozen. For Ni (211) and Ni (111), a 10-layer (3 × 2) unit cell and a 4-layer (6 × 4) unit cell were employed, respectively. The lower half of Ni slabs were frozen. The (100) facet of LSNT was chosen because the exsolution of Ni particle from LSNT was observed in (100) and (001) directions [15]. The LSNT (100) surface terminated by B-site atoms was cleaved from the optimized bulk. Then, the relaxed surface slab was employed to construct LSNT-Ni$_9$. The thickness of the vacuum layer in Ni (111) and Ni (211) models is 15 Å, and the vacuum was increased to 20 Å in the LSNT (100) model for the in-situ exsolved Ni$_9$ particle.

3. Results and discussion

3.1. Characterization of catalysts

The bulk phase structure of the LSNT catalysts was characterized by XRD. The as-synthesized LSNT catalyst shows diffraction peaks at 2θ = 22.7°, 32.4°, 39.9°, 46.5°, 52.3°, 57.8°, 67.8° 72.6°, and 77.2° (Fig. 1a), which can be assigned to a typical perovskite type cubic structure with a space group of Pm-3 m (JCPDS #036–734). The crystallite structure is further confirmed by the homogeneous distribution of various elements, including La, Sr, Ni, and Ti in the STEM-EDX mapping results, as well as the high-resolution TEM images, which displays a lattice distance of 0.387 nm, corresponding to the (111) plane of the perovskite phase (Fig. 1b). No substantial changes in the diffraction peaks associated with the perovskite phase of the LSNT powders occurred either after reduction in H$_2$ at 900 °C or subject to the PDH reaction at 600 °C for over 10 h, suggesting that the perovskite structure remained intact during these treatments. Nevertheless, a close inspection of the XRD patterns reveals that weak diffraction peaks at around 43.2° corresponding to the nickel phase emerged after either reduction pretreatment or extended exposure to reaction conditions, suggesting that reduction-induced exsolution occurred during these two processes. The formation of exsolved Ni was confirmed by high resolution TEM characterization, which clearly shows the Ni particle–perovskite socket resulting from the nucleation of reduced Ni atoms from the LSNT substrate (Fig. 1c), similar to that reported previously [39]. Nevertheless, no discernable Ni nanoparticles from the reduction-induced exsolution of Ni can be observed from the STEM-EDX mapping (Figs. 1d and S1), probably due to the relatively low resolution. The TEM images of the LSNT samples before and after reaction (Fig. S2) display similar particle morphologies and size distributions of the perovskite phase, in good agreement with the XRD results.

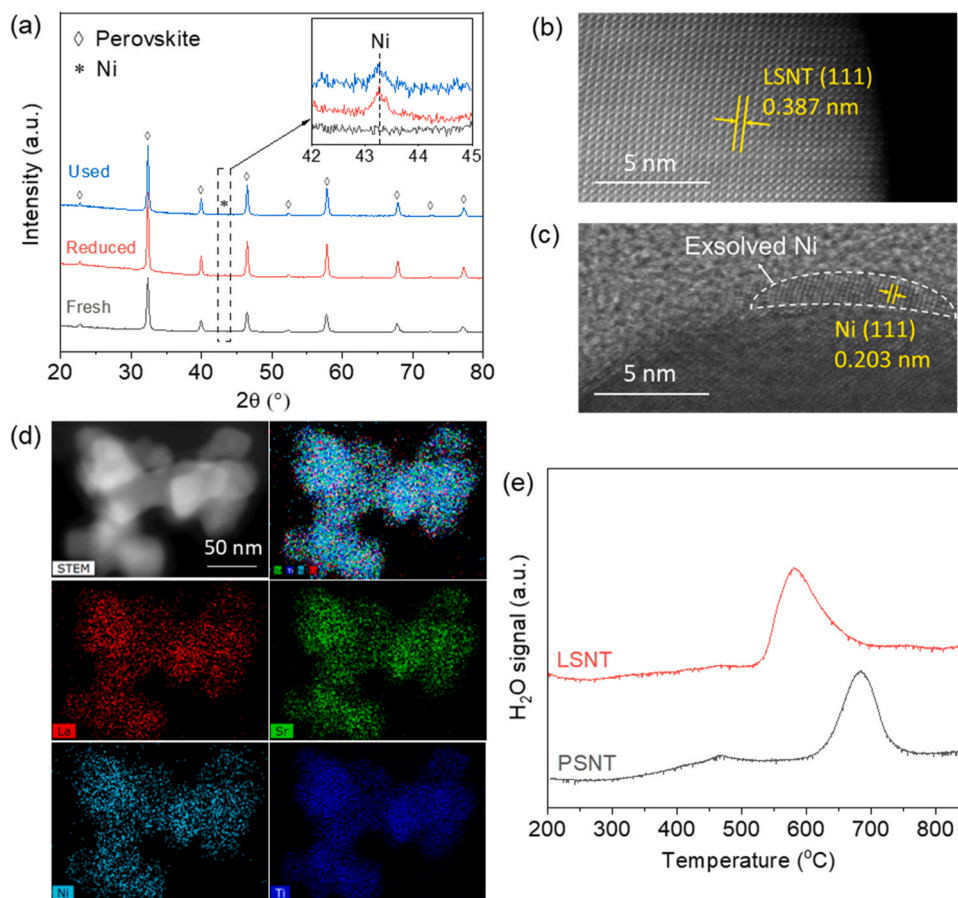The reducibility of the LSNT catalyst was investigated by H$_2$-TPR

Fig. 1. Characterization of the LSNT catalysts: (a) XRD patterns of the as prepared, reduced, and used LSNT catalysts, high-resolution TEM images of (b) fresh and (c) reduced LSNT catalyst, (d) STEM image and elemental mapping of reduced LSNT catalyst, (e) H_2-TPR profiles of LSNT and PSNT catalysts.

experiments. The reduction profile (Fig. 1e) shows a major peak at around 582 °C associated with the reduction of Ni^{2+} in the surface layer to Ni^0. Similar H_2-TPR profiles have recently been reported for LSNT materials with different reduction temperatures, which should be mainly due to different elemental compositions [47,50]. For comparison, the TPR profile of a PSNT catalyst with the same elemental composition as the LSNT shows a reduction peak at 683 °C with a small peak at 467 °C. The relatively lower temperature of the reduction peak for LSNT points to its better surface redox capability as compared with that for PSNT.

XPS analysis was performed to examine the chemical state of various surface species on the LSNT catalyst before and after reaction. In the C 1 s region (Fig. 2a), two peaks at the BE of 284.6 eV and 279.5 eV were detected on the as-prepared sample. The former peak is attributed to the adventitious carbon [51,41], whereas the latter should stem from the Sr $3p_{1/2}$ signal [52]. After reaction, there was a significant increase in the intensity of the C 1 s signal by almost an order of magnitude with the peak position shifting to lower BE at ca. 284.0 eV, which can be ascribed to the chemisorbed C species [56,18,57] accumulated on the surface during the PDH reaction. The La 3d spectra (Fig. 2b) exhibit two sets of La $3d_{5/2}$ and $3d_{3/2}$ doublets with an energy separation of around 3.9 eV and a branching ratio of 1.5 resulting from contributions of several initial and final states. Both the BE of the La $3d_{5/2}$ peak and the characteristic energy split of the doublets point to a La^{3+} state, likely in oxide and/or hydroxide form [5,35]. Due to the relatively weak intensity of the signals and the overlap of the main $Ni2p_{3/2}$ features with the $La3d_{3/2}$ peak, it is difficult to reliably determine the BE of Ni 2p peaks. Therefore, peak fitting efforts were not attempted to avoid misleading conclusions on the oxidation state of Ni species. The Ti 2p feature (Fig. 2c) exhibits a symmetrical signal with the $2p_{3/2}$ component at 457.4 eV,

corresponding to the Ti^{4+} state on the as-prepared LSNT catalyst [52]. No substantial changes in the BE of the Ti $2p_{3/2}$ peak occurred after exposure to reaction conditions except for the relatively lower intensity, suggesting negligible reduction of surface Ti oxide and deposition of C species on the surface from the reaction, which is consistent with the C 1 s XPS results.

The O1s spectrum of the as prepared LSNT catalyst showed a major peak at 529.2 eV with a shoulder at ca. 531.2 eV (Fig. 2d). This peak is typically assigned to the surface lattice oxygen ($O_{lattice}$) of the mixed metal oxides, while the peak at higher BE is attributed to oxygen species in the vicinity of oxygen vacancies (O_{vac}) or surface hydroxyl groups [5,35,10]. After reaction, there is a notable decrease in the overall intensity of the O1s signal accompanied by a significant increase in the fraction of the O_{vac} peak area from 23% to 55%. This result suggests that in addition to the carbon deposition, the LSNT catalyst also underwent substantial reduction during the PDH reaction, which is expected in view of the non-oxidative reaction conditions.

To probe the chemical states of surface Ni species, *in situ* CO adsorption DRIFTS experiments were performed on the LSNT catalyst before and after reaction. For the fresh LSNT sample, the CO adsorption band centered at ca. 2090 cm^{-1} is assigned to carbonyls bonded to partially reduced Ni^+ sites [20], indicating the presence of oxygen vacancies even on the as prepared catalyst, which is consistent with the O1s XPS results (see Fig. 2d). The absorption band at ca. 2200 cm^{-1} belongs to the stretching vibration of CO on Ni^{2+} sites [43]. The IR spectrum on the catalyst after exposure to reaction conditions for 1 h shows a stronger asymmetric absorption band in the range of 2000 – 2120 cm^{-1} with a peak at 2108 cm^{-1}, attributable to dicarbonyls bonded to Ni^+ as well as linear CO adsorbed on metallic Ni sites [20,43, 31]. This result revealed that the catalyst underwent further partial
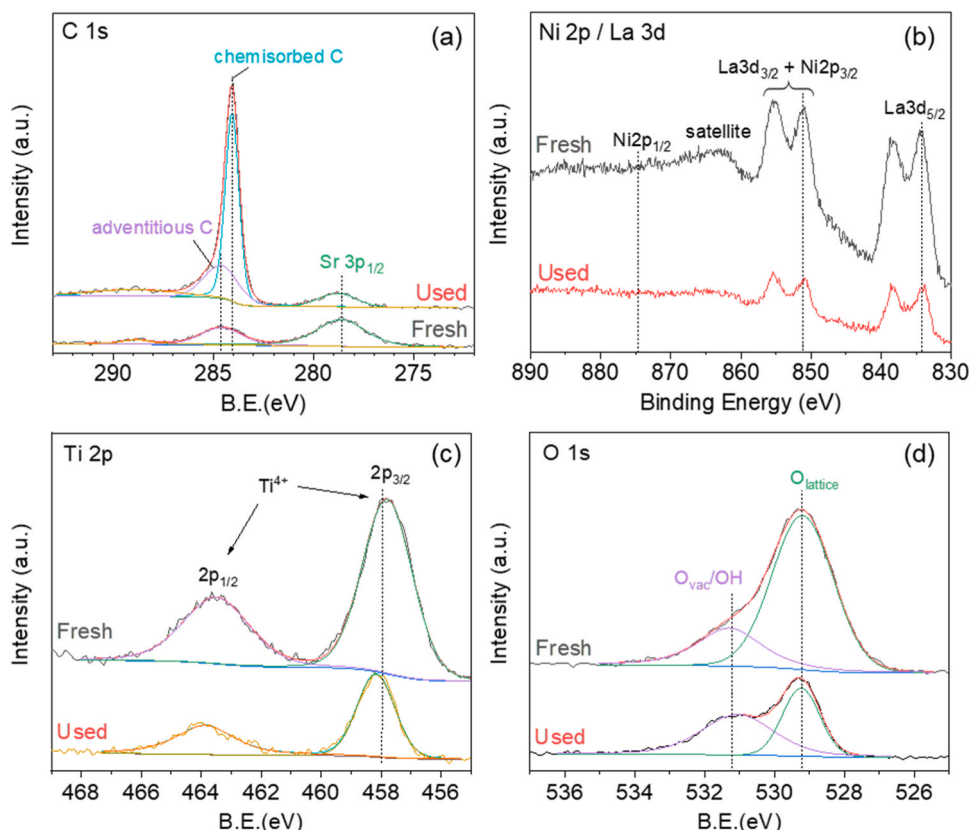
Fig. 2. XPS spectra of LSNT catalysts before and after reaction: (a) C 1 s, (b) Ni 2 p / La 3 d, (c) Ti 2 p, and (d) O 1 s.

reduction under reaction conditions. After reaction for 10 h, a broad absorption feature appeared in the range of 1900 – 2000 cm^{-1} with the peak centered around 1950 cm^{-1} (Fig. 3), which can be ascribed to the carbonyls strongly adsorbed on multiple metallic Ni atoms in a bridged configuration [14,3,36], pointing to the enhanced degree of reduction of Ni oxide with extended reaction. The progressive reduction of Ni as revealed by the *in situ* CO adsorption DRIFTS experiments suggests that partially reduced Ni species may be responsible for the catalytic activity of the LSNT catalyst.

To assess the compatibility of the LSNT catalyst under SOC working conditions, the conductivity was also measured at different temperatures and hydrogen partial pressures. The results (Fig. S3) show that the conductivity increases with the temperature. A conductivity of 33.3 and

43.2 S m^{-1} at 600 °C and 700 °C was achieved for the LSNT catalyst in pure hydrogen, respectively, which is significantly higher than that of PSNT (24 S m^{-1} at 700 °C) as reported previously [48].

3.2. Catalytic performance in fixed bed flow reactor

The catalytic performance of the LSNT catalyst was initially evaluated in a conventional fixed bed flow reactor after being reduced at 900 °C. The results (Fig. 4a) show that the LSNT catalyst exhibits a rather high initial propane conversion of about 90%, followed by a rapid decline in the first 2 h of reaction and then reached a steady state after about 5 h. The evolution of the selectivity of olefin products (ethylene and propylene) underwent an opposite trend to that of propane conversion, namely, almost no olefin products initially. The rapid decrease in propane conversion is accompanied by a rapid increase in the olefin selectivity, which approached a steady state after reaction for about 9 h. The carbon balance based on the gaseous products shows a similar evolution trend as that of olefin selectivity, indicating that there was a significant amount of non-gaseous products at the beginning of the reaction, most likely comprising of carbon deposits as well as non-volatile high hydrocarbons.

A detailed analysis of the gaseous products revealed that methane was the dominant product at the beginning of the reaction (Fig. 4b). Apart from ethylene and propylene, a small amount of ethane ($<$10%) was also detected. The time-dependent change in methane fraction in the products closely resembles the propane conversion. The dramatic shift in both propane conversion and product selectivity points to the change in the dominant active sites for propane activation and conversion. The initially high propane conversion with almost exclusive formation of methane and carbon deposition is characteristic of the catalytic behaviour of metallic Ni, which is highly active in C-C bond cleavage leading to low selectivity to dehydrogenation products. The metallic Ni species which could be formed through a so-called
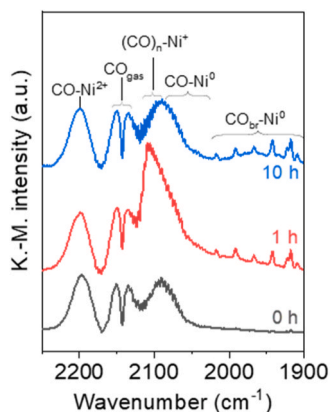

Fig. 3. *In situ* DRIFTS spectra of CO adsorption on the LSNT catalyst before and after reaction. CO_{gas} – gas phase CO, CO_{br} – bridged CO. The intensities are normalized by the peak at 2200 cm^{-1}.
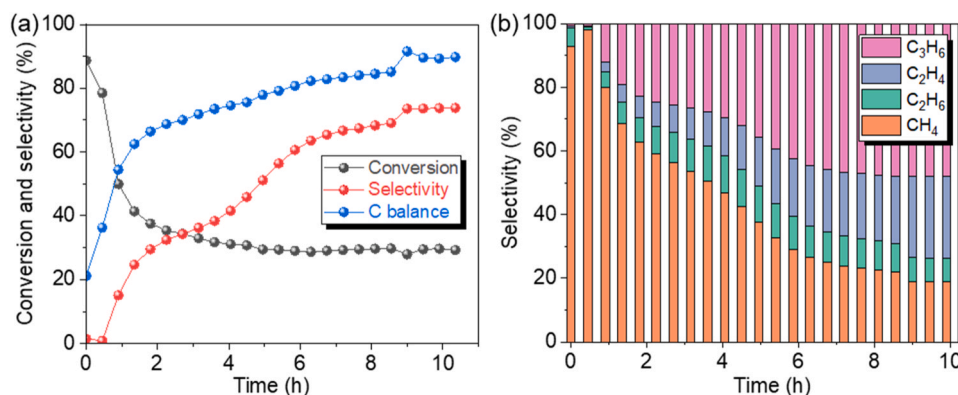
Fig. 4. Catalytic performance of the LSNT catalyst in PDH reaction as a function of reaction time: (a) propane conversion, olefin selectivity, and carbon balance, (b) product distribution. Reaction conditions: 100 mg catalyst, 600 °C, $C_3H_8/H_2/Ar=5/5/40$, total flow rate 50 mL min^{-1}.

exsolution process induced by the high temperature reduction pre-treatment, which is commonly seen in non-stoichiometric perovskite materials, especially with A-site deficiencies [48,32,49,40]. The rapid activity loss in the first 2 h should result from the blockage of metallic Ni sites by the carbon deposits, commonly known as the primary cause for the deactivation of Ni catalysts in hydrocarbon conversion reactions [53,54]. The remaining activity with a relatively stable conversion of around 30% may originate from the interfacial sites between metallic Ni and the perovskite substrate. Note that no measurable carbon oxide products including CO and CO_2 were detected in the product stream at 600 °C or lower temperatures, as the BZY-based electrolyte material demonstrates almost pure proton conducting behavior at lower temperatures (<600 °C) [23]. BZY electrolyte materials are known to be susceptible to CO_2 poisoning, which is a critical concern in the electrochemical processing of hydrocarbons. The relatively lower operating temperature in this work enables a real non-oxidative atmosphere, i.e., no oxygen containing species at the anode side during the electrochemical operations, thus eliminating CO/CO_2 formation from the oxidation of propane.

To further improve the performance, the LSNT catalyst was modified by either replacing or adding metal ions in the A- or B- site of the perovskite structure. Accordingly, a series of catalysts including $La_{0.3}Sr_{0.7}Co_{0.07}Ti_{0.93}O_{3-\delta}$ (LSCT), $La_{0.33}Sr_{0.67}Al_{0.08}Ti_{0.92}O_{3-\delta}$ (LSAT), $BaTiO_{3-\delta}$ (BTO), $(La_{0.3}Sr_{0.7})_{0.9}Ni_{0.3}Mo_{0.1}Ti_{0.6}O_3$ (LSNMT), and $(PrBa)_{0.95}Fe_{1.6}Ni_{0.3}Mo_{0.1}O_{6-\delta}$ (PBFNM) were synthesized by the same method as that for LSNT and tested in a fixed bed flow reactor. The catalytic performance of these catalysts was compared with that of LSNT under the same conditions (Fig. 5). For most of these catalysts, the propane conversion was below 10% with a selectivity of >80% to the olefin products. In contrast, a propane conversion of 29.7% was

obtained on the LSNT catalyst at 600 °C, significantly higher by a factor of up to 7 than that of the modified catalysts except for the LSNMT catalyst. The previously reported PSNT catalyst [48] has a propane conversion of 11.5% under the conditions adopted in this work, which is almost three times lower than that for the LSNT catalyst. The corresponding olefin selectivity on the LSNT catalyst was 73.8%, which is relatively lower than the rest of the catalysts. In principle, a direct comparison of selectivity should be made at a comparable conversion level. Although the addition of Mo to the LSNT resulted in dramatic increase in propane conversion (>95%), a negligible amount of olefin products was detected. Overall, the LSNT catalyst exhibits the best overall performance among all the perovskite catalysts tested.

In addition to mixed-metal-oxide perovskite type catalysts, an industry-relevant PtGa alloy catalyst supported on ZSM-5 zeolite material was also synthesized by the incipient wetness impregnation method and tested under the same conditions for comparison. The propane conversion over the PtGa/ZSM-5 catalyst was measured to be 30.7% at 600 °C under pseudo steady state (Fig. 5), which is comparable to that on the LSNT catalyst, while the olefin product selectivity of 77.1% is relatively higher. This comparison further confirms that LSNT is among the most active catalysts for the PDH reaction.

3.3. Effect of catalyst integration method and applied current density on the performance of catalyst-integrated p-SOC

To investigate the catalyst performance on p-SOC, a batch of cathode supported button cells was first fabricated. A representative SEM image of the cross section of the cells is shown in Fig. S5a. The cell consists of a thin BZY20 electrolyte (~10 μm), the NiO-BZCYYb cathode support (~400 μm) with a cathode functional layer (CFL, ~25 μm), and a porous PBFM + LSNT anode (~70 μm). In a typical electrochemical performance evaluation measurement, propane is fed to the catalyst-incorporated cathode and dehydrogenated to propylene, electrons, and protons. Under an applied potential or current, the protons are immediately transported through the electrolyte and recombine with electrons at the cathode side to produce H_2. The electrochemical performance was first evaluated under the fuel cell mode. A peak power density of 193 mW cm^{-2} could be achieved at 600 °C (Fig. S5b), which is relatively lower than that using H_2 as the fuel (~306 mW cm^{-2}). The corresponding ohmic and polarization resistance is 0.483 and 0.153 Ω cm^2 at 600 °C, respectively. Both the Ohmic and polarization resistances decrease at elevated temperatures (Fig. S5c).

The performance of p-SOCs with integrated catalysts could be significantly affected by the method of catalyst incorporation onto the electrode. Accordingly, the effect of different methods for integration of the LSNT catalyst onto the electrode was investigated. The LSNT catalyst was first integrated into the button cell by the infiltration method. Fig. 6 shows the elemental mapping results of the PBFM electrode after
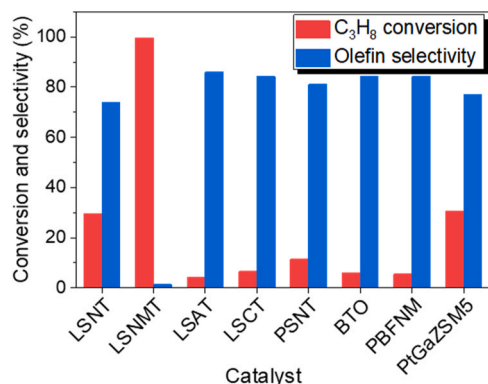

Fig. 5. Comparison of propane conversion and olefin selectivity over different catalysts. Reaction conditions: 100 mg catalyst, 600 °C, $C_3H_8/H_2/Ar=5/5/40$, total flow rate 50 mL min^{-1}.
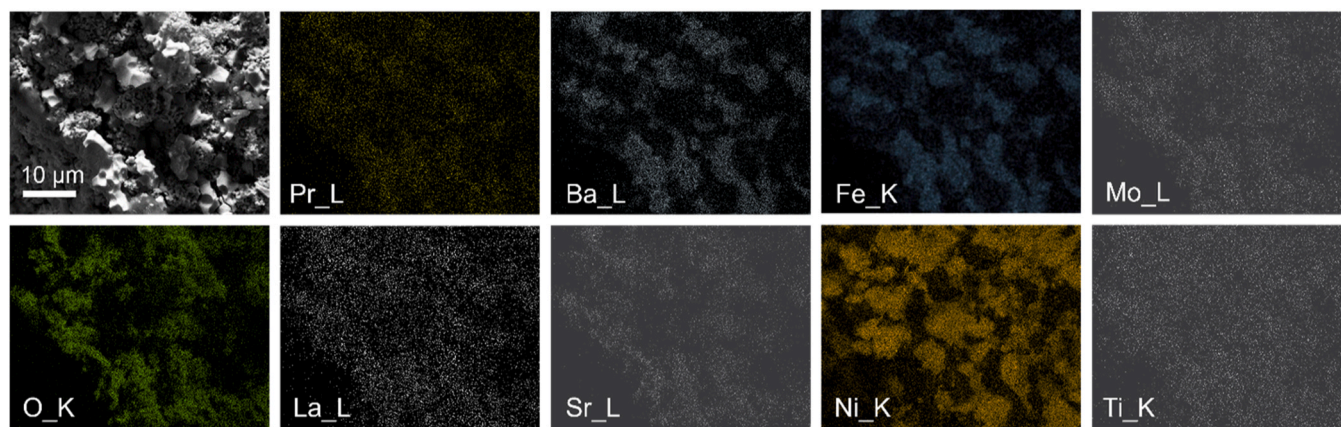
Fig. 6. SEM-EDX of the PBFM electrode infiltrated with the LSNT catalyst.

infiltration of the LSNT catalyst. Each element in the catalyst is homogeneously distributed throughout the PBFM electrode. Analysis of the weight change after repeated infiltration procedures indicates that the LSNT catalyst loading can reach >75 wt%.

The electrochemical performance of the cell with an infiltrated catalyst was first evaluated before introducing the propane feed gas to ensure stable operation of the cell under certain applied voltage or current density since too high voltages may lead to electrolyte breakdown. As displayed in Fig. 7a, the catalyst integrated cell showed good stability under cyclic applied potentials between -0.2 V and -0.4 V, with a corresponding current density of ca. 40 mA cm^{-2} and 70 mA cm^{-2}, respectively. The catalytic performance of the infiltrated LSNT catalyst was then evaluated under different applied current densities (Fig. 7b). There was a slight increase in propane conversion, from 10.2% to 10.7%, as the current increased from 0 to 40 mA cm^{-2} with negligible changes in the olefin product selectivity. The rather limited increase in propane conversion may originate from the small current density as well as the low propane conversion value, which determines the amount of proton transfer. Note that the propane conversion (~10%) is significantly lower than that obtained under thermal catalytic conditions (>30%) in the fixed bed flow reactor. This is mainly due to the relatively lower amount (~25 mg) of catalyst available for the reaction, which is limited by the infiltration method. To examine if the PBFM electrode contributes to the PDH activity, additional experiments have also been performed under the same conditions after the same reduction pretreatment for LSNT catalyst. The results showed that the propane conversion over PBFM is less than 4% at 600 °C over 15 h (Fig. S4), which is almost negligible compared to that of LSNT (~30% under steady state).

The LSNT catalyst was also added onto the PBFM-BZY electrode as a second layer by a brush painting method. Note that a layer of silver paste was first applied onto the PBFM electrode as the current collector prior to the integration of the LSNT catalyst layer. A representative SEM image of the catalyst-integrated cell is shown in Fig. S6. The electrochemical performance of the cell with coated catalyst was also evaluated under different applied current densities (Fig. 8a). With a constant applied current density of ca. 30, 60, and 90 mA cm^{-2}, a stable voltage of 0.37, 0.89, and 1.10 V was obtained, respectively. The catalytic performance of the LSNT catalyst in terms of propane conversion, olefin selectivity, and H$_2$ production rate as a function of the applied current density are shown in Fig. 8b-d, respectively. The results indicate that higher conversion of propane can be achieved by increasing the applied current density. The propane conversion increases steadily from 47% to 53% as the applied current increases from 30 to 90 mA cm^{-2}, while the olefin product selectivity only slightly decreases from 78% to 77%. The product distribution was almost unchanged upon the increased applied current density (Fig. 8c). Meanwhile, the hydrogen production rate was substantially enhanced from 1.27 to 1.96 mL min^{-1} (Fig. 8d).

The enhanced propane conversion over LSNT catalyst-loaded cell under applied current may originate, at least in part, from the electrochemical activation of propane, namely, the electrochemical promotion of the catalytic PDH reaction. Alternatively, the promotional effect may also result directly from the shifting of reaction equilibrium to the right direction due to the enhanced hydrogen separation from the product mixture via proton transfer from the anode to the cathode side under the applied current. In this scenario, the propane conversion proceeds via a tandem mechanism involving a thermal catalytic PDH reaction on the LSNT catalyst layer, followed by electrochemical activation of hydrogen
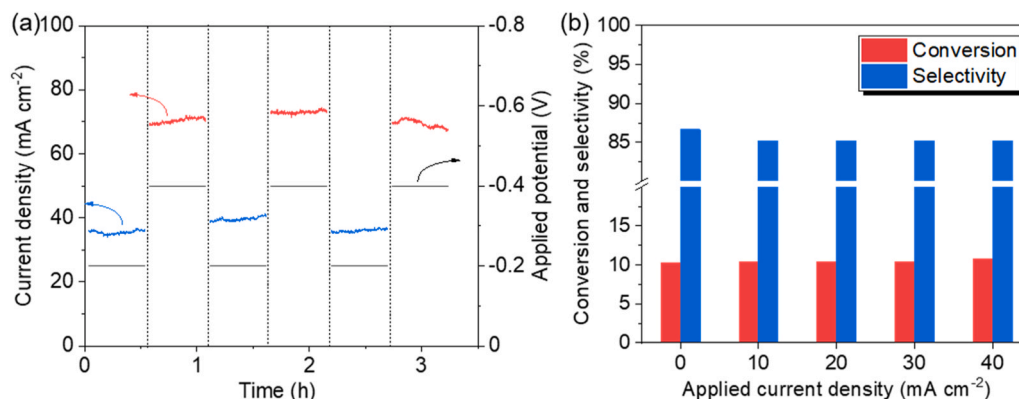

Fig. 7. (a) Electrochemical performance of the cell PBFM | BZY | BZCYYb-NiO infiltrated with LSNT catalyst under H$_2$ | 2% H$_2$ gradient. (b) C$_3$H$_8$ conversion and olefin selectivity as a function of applied current on the infiltrated LSNT catalyst.
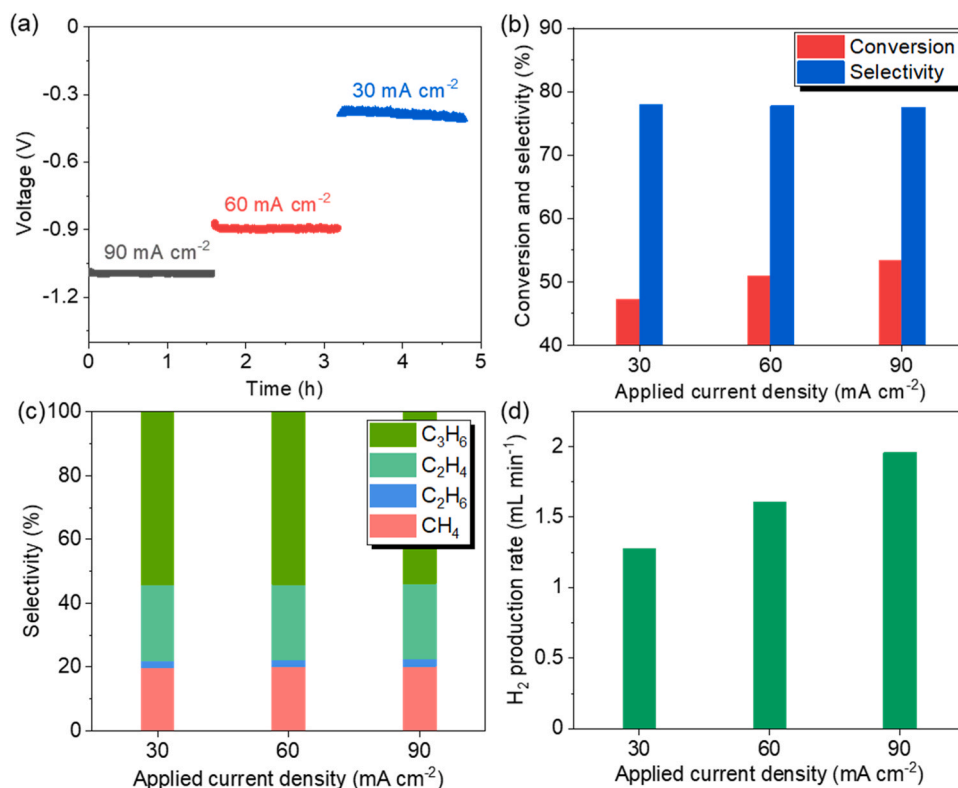
Fig. 8. (a) Electrochemical performance (b) C_3H_8 conversion and olefin selectivity, (c) product distribution, and (d) H_2 production rate as a function of applied current densities on cell PBFM-BZY | BZY | BZCYYb-NiO coated with LSNT catalyst.

on the cathode to form protons. It is reasonable to speculate that both the formation of protons and their ensuing transfer through the electrolyte membrane could be accelerated by the applied current density. However, it is difficult to explicitly distinguish the electrocatalytic mechanism from the tandem reaction pathway solely based on the experimental evidence obtained here.

3.4. Effect of water vapor on the catalyst performance

The effect of water vapor in the feed gas on the catalyst performance under an electrochemical environment was also investigated. The reaction was initially operated in dry propane with an applied current density of 100 mA cm^{-2} until a relatively steady state was reached and then the reaction was switched to the feed gas containing 10% H_2O. There was a rapid decline in propane conversion in the first 3 h of

Fig. 9. Effect of water vapor on the propane conversion, olefin selectivity, and olefin yield over LSNT catalyst at 600 °C under 100 mA cm^{-2}, (cathode feed 2% H_2, anode feed 10%C_3H_8 + 10%H_2O + 80%Ar).

reaction accompanied by gradual increase in olefin selectivity (Fig. 9). As a result, the olefin yield decreased from 29% to 24% after reaction for 5 h, most likely caused by the carbon deposition. Upon the introduction of 10% H_2O into the feed gas, there was a step increase in propane conversion with a moderate decrease in olefin selectivity and then remained in a steady state for over 6 h. As a result, the olefin yield increased back to 29% and remained constant. These results clearly indicate that the addition of water in the feed gas could suppress the coke formation and greatly enhance the catalyst stability in PDH reaction under an electrochemical environment. The improved stability of the catalyst performance in the presence of water vapor in the feed gas should be attributed to the fact that water can suppress the carbon deposition during reaction by directly reacting with coke at the operating temperature via the reaction C + H_2O → CO + H_2. This is also supported by the observation that propane conversion as well as the olefin product selectivity was essentially restored to the original level upon the addition of water, which indicates that the blocked active sites by the carbon deposits were fully recovered in the presence of water. Note that adding water vapor in the feed gas may also benefit the electrochemical performance of the p-SOC by facilitating the proton formation. A recent work [48] has shown that the hydrogen formation rate could be substantially enhanced by increasing the water content in the propane feed gas.

3.5. Effect of sulfur impurities on the catalyst performance

Apart from the effect of catalyst composition and reaction conditions, other factors such as contaminants in the feed gas may also have a pronounced impact on the catalyst performance in PDH reactions. In practice, commercial grade propane gases are usually odorized by blending with trace amounts up to 300 ppm of sulfur compound such as ethyl mercaptan [1], which may potentially affect the activity, selectivity, and stability of LSNT catalysts in the dehydrogenation reaction. Accordingly, a control experiment was conducted on the LSNT catalyst
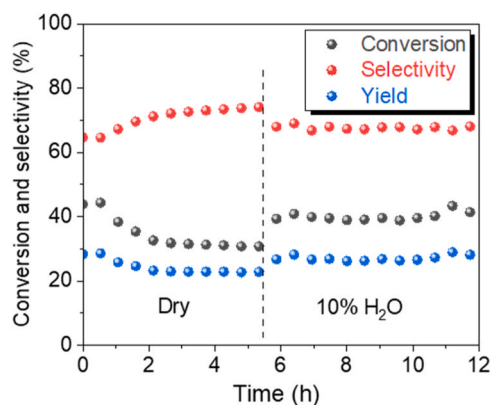
using an odorized propane gas as the feed gas. The results (Fig. 10a) showed that the activity and selectivity of the LSNT catalyst are substantially affected by the sulfur impurities. Upon switching from clean propane to the odorized feed gas, the propane conversion increased from 31% to ~40%, while the olefin selectivity decreased from 81% to 68%. As a result, there was a slight net increase in the olefin yield from about 25–27%. According to the product analysis shown in Fig. 1b, the presence of sulfur in the feed gas leads to more ethane production at the expense of propylene (Fig. 10b). In addition, the results also clearly indicate that the LSNT catalyst exhibits excellent stability in the catalytic performance throughout the experiment, essentially unaffected by the presence of sulfur contaminants in the feed gas. Based on these results, we infer that the sulfur containing compound in the feed gas may adsorb on the surface of the LSNT catalyst and alter the chemical environment or electronic properties of the Ni active sites, most likely at the interface between exsolved Ni and LSNT support. This would result in enhanced activity and altered reaction mechanisms, which account for the increased ethane selectivity. A detailed mechanistic investigation into this aspect, however, is beyond the scope of this study and will be reported elsewhere.

3.6. Nature of active sites for PDH reaction

To understand the reaction behavior of LSNT catalyst in PDH reaction (Fig. 4) and gain insights into the nature of active sites, DFT calculations were performed to investigate PDH reaction over three possible active sites on the *in situ* exsolved LSNT: (i) Ni nanoclusters/nanoparticles, (ii) LSNT support, and (iii) the Ni-LSNT interface. As shown in Fig. 11a, Ni (211) and Ni (111) represent the terrace and step sites of the metallic nickel catalyst. LSNT represents the pristine LSNT support, whereas LSNT-Ni$_9$ was used to depict the interfacial sites. AIMD simulations were used to relax the Ni$_9$ cluster supported on LSNT. Initially, nine ordered Ni atoms were placed on clean LSNT surface, cleaved from the optimized LSNT bulk (Fig. S8).

The valence charges of surface Ni atoms in four different models were first calculated by Bader charge analysis to determine the electronic properties of Ni atoms in the catalyst system. The results (see Table S1) indicate that the Ni atoms in the LSNT lattice are charge deficient by -1.30 e relative to free Ni atoms, whereas the Ni atoms in the Ni cluster supported on LSNT (LSNT-Ni$_9$) exhibit varying electronic states depending on their locations in the cluster. As expected, the Ni atoms at the interface, including the surface lattice Ni atoms in the LSNT substrate, display different degrees of charge deficiency (Fig. 11b), pointing to substantial charge transfer from the Ni cluster to LSNT at the boundary between the Ni$_9$ cluster and the LSNT support. On the other hand, charge accumulates to different extents on Ni^1, Ni^4, and Ni^8 atoms (Fig. 11a and Table S1), which are not directly bonded with the lattice

oxygen atoms in the LSNT substrate.

It is generally accepted that the activation of the first C-H bond is the rate-limiting step of light alkane dehydrogenation reactions [8]. To understand the activity of LSNT catalyst in PDH, the transition states involved in the first C–H bond activation were obtained (Fig. S9) and the adsorption energies (E_{ad}) of selected species, including C$_3$H$_8$, 1-C$_3$H$_7$, H, and C$_3$H$_6$, are displayed in Fig. 11c. Basically, the E_{ad} of all PDH intermediates show the same trend of LSNT-Ni$_9$ $\approx$ Ni (211) > Ni (111) > LSNT. Stronger C$_3$H$_8$ adsorption and higher E_{ad} of 1-C$_3$H$_7$ and H facilitate the activation of the first C-H bond. On LSNT-Ni$_9$, C$_3$H$_8$ adsorption prefers the top metallic Ni atoms. As illustrated in Fig. S10, C$_3$H$_8$ shows the most substantial charge transfer with the top atoms on LSNT-Ni$_9$ among all models, consistent with its higher E_{ad} values.

The potential energy profiles of PDH and C-C bond cleavage were produced to reveal the energy landscape of elemental reaction steps on different model surfaces. The results (Fig. 11d) show that the energy barrier for the first C-H bond activation is the lowest on LSNT-Ni$_9$ (0.73 eV), followed by Ni(211) (0.75 eV), Ni(111) (0.94 eV), and LSNT (1.38 eV). In addition, the first and second dehydrogenation steps are exothermic on LSNT-Ni$_9$ benefitting from the strong binding of H on LSNT-Ni$_9$. It is widely believed that Ni sites suffer from carbon deposition due to active C-C bond cleavage, which is responsible for the low C$_3$H$_6$ selectivity. DFT calculations suggest that the C–C bond cleavage energy barrier (1.86 eV) on LSNT-Ni$_9$ is higher than that on Ni(211) (1.42 eV) and Ni (111) (0.82 eV). The high barrier and energy change of LSNT-Ni$_9$ reflect the high resistance to C-C bond cracking for PDH. Since the E_{ad} of C$_3$H$_6$ and atomic H are similar on LSNT-Ni$_9$ and Ni(211) (Fig. 11c), the desorption of gaseous C$_3$H$_6$ and H$_2$ will be competitive on these two surfaces. Nevertheless, the high barrier to C-C bond cracking on LSNT-Ni$_9$ makes it more selective in propylene formation than on pure Ni catalysts.

The vibrational analysis of CO adsorption on various model surfaces was also performed to corroborate the CO absorption bands observed in the *in situ* DRIFTS experiments (Fig. 3). The DFT-calculated frequency for gas phase CO is 2128 cm^{-1}, which is close to the *in situ* DRIFTS result. In addition, the DFT-calculated vibrational frequencies of adsorbed CO on different model surfaces follow the order of Ni^{2+} (LSNT) > Ni$^+$ (LSNT-Ni$_9$) > Ni^0 (Fig. S11), also in good agreement with the experimental results. Note that there are some discrepancies between the theoretical and experimental frequency values, possibly due to the coverage effect. Additional DFT calculations showed that the vibrational frequency of CO may vary from 1760 cm^{-1} at 6.25% coverage to 1997 cm^{-1} at 100% coverage on the *hcp* site of the Ni(111) surface (see Fig. S12).

Based on the DFT calculation results discussed above, the underlying mechanism behind the reaction behavior in Fig. 4 can be interpreted as follows. During the first 2 h of reaction, propane conversion primarily
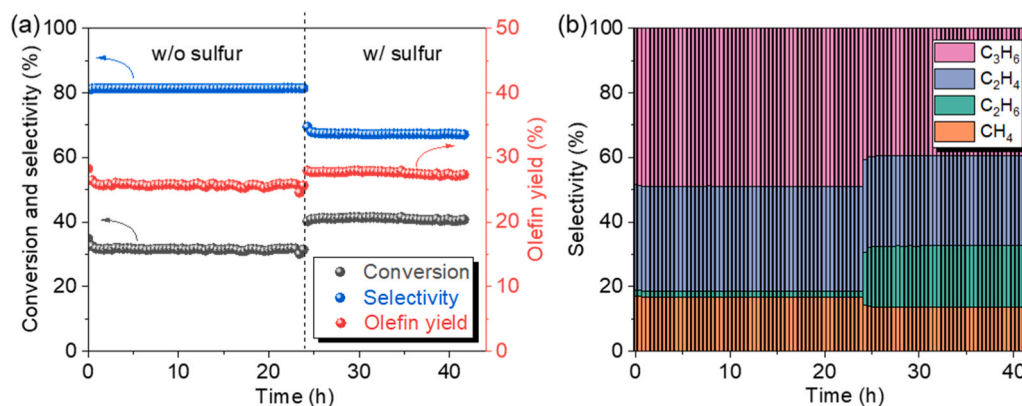

Fig. 10. Effect of sulfur contaminants on the catalytic performance of the LSNT catalyst in PDH reaction at 600 °C: (a) propane conversion, selectivity, and olefin yield and (b) product distribution as a function of time on stream.
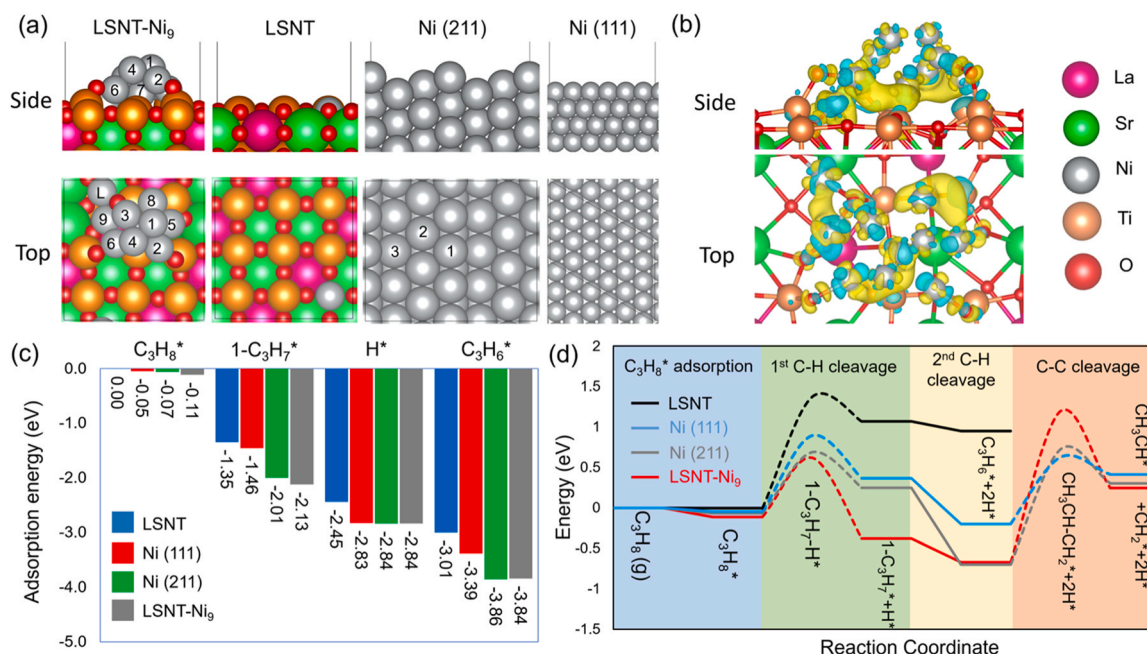
Fig. 11. (a) Catalyst models for LSNT-Ni$_9$, LSNT, Ni(211), and Ni(111). The numerical labels indicate the atomic positions for the valence charges summarized in Table S1. (b) Charge density difference of LSNT due to the presence of Ni$_9$ cluster, yellow and cyan represent charge accumulation and depletion with an isosurface level of 0.001 e/Bohr^3, respectively. (c) Adsorption energies of propane (C$_3$H$_8$), 1-propyl (1-C$_3$H$_7$), and H. (d) Potential energy profiles for propane dehydrogenation and C–C bond scission. The dashed lines indicate energy barriers. La, Sr, Ni, Ti, and O atoms are shown in wine, green, silver, orange, and red, respectively.

took place on highly active but less selective metallic Ni sites, leading to high propane conversion but negligible olefin formation. The products were dominated by deep dehydrogenation products such as carbon deposits, which blocked the metallic Ni active sites and resulted in rapid loss of activity. After reaction for 2 h, the interfacial sites between Ni clusters and LSNT substrate became the predominant active sites for propane conversion with high selectivity to olefin products until a steady state was reached.

4. Conclusion

In this work, we demonstrate a novel electrochemical process for propane conversion to produce propylene and high-purity hydrogen in a proton-conducting solid oxide electrochemical cell system. The highly efficient PDH reaction is enabled by a Ni/La co-doped strontium titanate perovskite catalyst, which shows high conductivity and excellent catalytic performance even comparable to the conventional Pt-alloy based thermal catalysts. The high catalytic performance is accounted for by the good surface redox properties and the formation of highly active *in situ* exsolved Ni species during the PDH reaction. The trace amount of sulfur impurities in the propane feed gas has no significant influence on the catalytic performance and stability of the LSNT catalyst. Propane conversion and hydrogen production rate can both be enhanced by applying current on the electrochemical cell, presumably via an electrocatalytic effect or accelerated hydrogen separation from the product mixture that could shift the reaction equilibrium into the right direction. Adding a certain amount of water vapor in the feed gas during electrochemical operations results in improved catalyst stability by suppressing the coke formation, which is a major cause for catalyst deactivation in the PDH reaction. Both the effects of water vapor and sulfur impurities have important implications for industrial application in terms of enhanced catalyst and reactor system stability, which is critical to lower the operational cost. DFT calculations revealed that the active sites for selective PDH reaction on the reduced LSNT catalyst are located at the interface between *in situ* exsolved Ni species and the LSNT support. Overall, this work shows the great potential of an alternative electrochemical pathway for intensified co-production of propylene and

hydrogen from commercial propane feedstock. The new reactor system can be readily coupled with clean energy sources such as nuclear power plants and renewable electricity. This work also provides a general approach for exploiting the potential of p-SOCs in sustainable chemical manufacturing. The electrocatalytic membrane reactor system described herein may find wide applications in reducing the energy consumption and carbon emissions for many energy- and carbon-intensive chemical processes not limited to non-oxidative hydrocarbon processing as exemplified in this work.

CRediT authorship contribution statement

Hao Deng: Writing – original draft, Visualization, Validation, Software, Methodology, Investigation, Formal analysis, Data curation. **Bin Liu:** Writing – review & editing, Supervision, Investigation, Formal analysis. **Fudong Liu:** Writing – review & editing, Supervision, Data curation. **Lucun Wang:** Writing – review & editing, Supervision, Resources, Project administration, Funding acquisition, Formal analysis, Conceptualization. **Daekun Kim:** Methodology, Investigation, Formal analysis, Data curation. **Yong Ding:** Methodology, Investigation, Formal analysis, Data curation. **Dong Ding:** Writing – review & editing, Supervision, Project administration, Funding acquisition. **Yuqing Meng:** Writing – original draft, Validation, Methodology, Investigation, Formal analysis, Data curation.

Declaration of Competing Interest

The authors declare that they have no known competing financial interests or personal relationships that could have appeared to influence the work reported in this paper.

Data availability

Data will be made available on request.

Acknowledgements

Appendix A. Supporting information

Supplementary data associated with this article can be found in the online version at doi:10.1016/j.apcatb.2024.124111.

References

[1] A.S. Afshar, S.R. Hashemi, M. Miri, P. Setayeshi, The optimization of effective factors on mercaptan extraction by alkaline solution, Pet. Sci. Technol. 31 (2013) 2364–2370.

[2] A. Akah, M. Al-Ghrami, Maximizing propylene production via FCC technology, Appl. Petrochem. Res. 5 (2015) 377–392.

[3] H.A. Aleksandrov, V.R. Zdravkova, M.Y. Mihaylov, P.S. Petkov, G.N. Vayssilov, K.I. Hadjiivanov, Precise identification of the infrared bands of the polycarbonyl complexes on Ni–MOR Zeolite by $^{12}C^{16}O–^{13}C^{18}O$ coadsorption and computational modeling, J. Phys. Chem. C. 116 (2012) 22823–22831.

[4] I. Amghizar, L.A. Vandewalle, K.M. Van Geem, G.B. Marin, New trends in olefin production, Engineering 3 (2017) 171–178.

[5] S. Amira, M. Ferkhi, A. Khaled, F. Mauvy, J.-C. Grenier, L. Houssiau, J.-J. Pireaux, Carbon-based lanthanum nickelate material $La_{2−x−y}Nd_xPr_yNiO_{4+\delta}$ (x= 0, 0.3, and 0.5; y= 0 and 0.2) as a bifunctional electrocatalyst for oxygen reduction in alkaline media, Ionics 25 (2019) 3809–3822.

[6] W. Bian, W. Wu, B. Wang, W. Tang, M. Zhou, C. Jin, H. Ding, W. Fan, Y. Dong, J. Li, Revitalizing interface in protonic ceramic cells by acid etch, Nature 604 (2022) 479–485.

[7] P.E. Blöchl, Projector augmented-wave method, Phys. Rev. B 50 (1994) 17953.

[8] S. Chen, X. Chang, G. Sun, T. Zhang, Y. Xu, Y. Wang, C. Pei, J. Gong, Propane dehydrogenation: catalyst development, new chemistry, and emerging technologies, Chem. Soc. Rev. 50 (2021) 3315–3354.

[9] D. Ding, Y. Zhang, W. Wu, D. Chen, M. Liu, T. He, A novel low-thermal-budget approach for the co-production of ethylene and hydrogen via the electrochemical non-oxidative deprotonation of ethane, Energy Environ. Sci. 11 (2018) 1710–1716.

[10] J. Druce, H. Tellez, M. Burriel, M. Sharp, L. Fawcett, S. Cook, D. McPhail, T. Ishihara, H. Brongersma, J. Kilner, Surface termination and subsurface restructuring of perovskite-based solid oxide electrode materials, Energy Environ. Sci. 7 (2014) 3593–3599.

[11] C. Duan, J. Huang, N. Sullivan, R. O'Hayre, Proton-conducting oxides for energy conversion and storage, Appl. Phys. Rev. 7 (2020) 011314.

[12] Y. Fan, X. Xi, J. Li, Q. Wang, M.-M. Li, L.-J. Wang, D. Medvedev, J.-L. Luo, X.-Z. Fu, In-situ exsolved FeNi nanoparticles on perovskite matrix anode for co-production of ethylene and power from ethane in proton conducting fuel cells, Electrochim. Acta 393 (2021) 139096.

[13] X.-Z. Fu, J.-L. Luo, A.R. Sanger, N. Danilovic, K.T. Chuang, An integral proton conducting SOFC for simultaneous production of ethylene and power from ethane, Chem. Commun. 46 (2010) 2052–2054.

[14] T.S. Galhardo, A.H. Braga, B.H. Arpini, J. Szanyi, R.V. Gonçalves, B.F. Zornio, C.R. Miranda, L.M. Rossi, Optimizing active sites for high CO selectivity during CO$_2$ hydrogenation over supported nickel catalysts, J. Am. Chem. Soc. 143 (2021) 4268–4280.

[15] H. Han, Y. Xing, B. Park, D.I. Bazhanov, Y. Jin, J.T. Irvine, J. Lee, S.H. Oh, Anti-phase boundary accelerated exsolution of nanoparticles in non-stoichiometric perovskite thin films, Nat. Commun. 13 (2022) 6682.

[16] G. Henkelman, H. Jónsson, A dimer method for finding saddle points on high dimensional potential surfaces using only first derivatives, J. Chem. Phys. 111 (1999) 7010–7022.

[17] G. Henkelman, B.P. Uberuaga, H. Jónsson, A climbing image nudged elastic band method for finding saddle points and minimum energy paths, J. Chem. Phys. 113 (2000) 9901–9904.

[18] S. Hofmann, R. Sharma, C. Ducati, G. Du, C. Mattevi, C. Cepek, M. Cantoro, S. Pisana, A. Parvez, F. Cervantes-Sodi, In situ observations of catalyst dynamics during surface-bound carbon nanotube nucleation, Nano Lett. 7 (2007) 602–608.

[19] B. Hu, Y. Wang, C. Xia, Effects of ceria conductivity on the oxygen incorporation at the LSCF-SDC-gas three-phase boundary, J. Electrochem. Soc. 162 (2014) F33.

[20] M. Kermarec, D. Delafosse, M. Che, An IR study of carbon monoxide fixation by Ni$^+$ ions obtained by photoreduction of a nickel-exchanged silica, Chem. Commun. (1983) 411–413.

[21] G. Kresse, J. Furthmüller, Efficiency of ab-initio total energy calculations for metals and semiconductors using a plane-wave basis set, Comput. Mater. Sci. 6 (1996) 15–50.

[22] G. Kresse, J. Hafner, Ab initio molecular dynamics for open-shell transition metals, Phys. Rev. B 48 (1993) 13115.

[23] K. Kreuer, Aspects of the formation and mobility of protonic charge carriers and the stability of perovskite-type oxides, Solid State Ion.-. 125 (1999) 285–302.

[24] J. Li, J. Hou, X. Xi, Y. Lu, M. Li, Y. Fan, L. Wang, L. Wang, X.-Z. Fu, J.-L. Luo, Cogeneration of ethylene and electricity in symmetrical protonic solid oxide fuel cells based on a $La_{0.6}Sr_{0.4}Fe_{0.8}Nb_{0.1}Cu_{0.1}O_{3−\delta}$ electrode, J. Mater. Chem. A 8 (2020) 25978–25985.

[25] M. Li, B. Hua, L.-C. Wang, J.D. Sugar, W. Wu, Y. Ding, J. Li, D. Ding, Switching of metal–oxygen hybridization for selective CO2 electrohydrogenation under mild temperature and pressure, Nat. Catal. 4 (2021) 274–283.

[26] M. Li, Y. Wang, Y. Wang, F. Chen, C. Xia, Bismuth doped lanthanum ferrite perovskites as novel cathodes for intermediate-temperature solid oxide fuel cells, ACS Appl. Mater. Interfaces 6 (2014) 11286–11294.

[27] S. Liu, Y. Behnamian, K.T. Chuang, Q. Liu, J.-L. Luo, A-site deficient $La_{0.2}Sr_{0.7}TiO_{3−\delta}$ anode material for proton conducting ethane fuel cell to cogenerate ethylene and electricity, J. Power Sources 298 (2015) 23–29.

[28] S. Liu, K.T. Chuang, J.-L. Luo, Double-layered perovskite anode with in situ exsolution of a Co–Fe alloy to cogenerate ethylene and electricity in a proton-conducting ethane fuel cell, ACS Catal. 6 (2016) 760–768.

[29] F. Liu, D. Ding, C. Duan, Protonic ceramic electrochemical cells for synthesizing sustainable chemicals and fuels, Adv. Sci. 10 (2023) 2206478.

[30] S. Liu, Q. Liu, X.-Z. Fu, J.-L. Luo, Cogeneration of ethylene and energy in protonic fuel cell with an efficient and stable anode anchored with in-situ exsolved functional metal nanoparticles, Appl. Catal. B: Environ. 220 (2018) 283–289.

[31] R. Ma, J. Gao, J. Kou, D.P. Dean, C.J. Breckner, K. Liang, B. Zhou, J.T. Miller, G. Zou, Insights into the nature of selective nickel sites on Ni/Al$_2$O$_3$ catalysts for propane dehydrogenation, ACS Catal. 12 (2022) 12607–12616.

[32] P.B. Managutti, S. Tymen, X. Liu, O. Hernandez, C. Prestipino, A. Le Gal La Salle, S. Paul, L. Jalowiecki-Duhamel, V. Dorcet, A. Billard, Exsolution of Ni nanoparticles from A-Site-deficient layered double perovskites for dry reforming of methane and as an anode material for a solid oxide fuel cell, ACS Appl. Mater. Interfaces 13 (2021) 35719–35728.

[33] M. Marinšek, K. Zupan, J. Maeek, Ni–YSZ cermet anodes prepared by citrate/nitrate combustion synthesis, J. Power Sources 106 (2002) 178–188.

[34] M. Methfessel, A. Paxton, High-precision sampling for Brillouin-zone integration in metals, Phys. Rev. B 40 (1989) 3616.

[35] S. Mickevičius, S. Grebinskij, V. Bondarenka, B. Vengalis, K. Šliužienė, B. Orlowski, V. Osinniy, W. Drube, Investigation of epitaxial LaNiO$_{3−x}$ thin films by high-energy XPS, J. Alloy. Compd. 423 (2006) 107–111.

[36] M. Mihaylov, K. Hadjiivanov, FTIR study of CO and NO adsorption and coadsorption on Ni-ZSM-5 and Ni/SiO$_2$, Langmuir 18 (2002) 4376–4383.

[37] H.J. Monkhorst, J.D. Pack, Special points for Brillouin-zone integrations, Phys. Rev. B 13 (1976) 5188.

[38] S.H. Morejudo, R. Zanón, S. Escolástico, I. Yuste-Tirados, H. Malerød-Fjeld, P.K. Vestre, W.G. Coors, A. Martínez, T. Norby, J.M. Serra, Direct conversion of methane to aromatics in a catalytic co-ionic membrane reactor, Science 353 (2016) 563–566.

[39] D. Neagu, V. Kyriakou, I.-L. Roiban, M. Aouine, C. Tang, A. Caravaca, K. Kousi, I. Schreur-Piet, I.S. Metcalfe, P. Vernoux, In situ observation of nanoparticle exsolution from perovskite oxides: from atomic scale mechanistic insight to nanostructure tailoring, ACS Nano 13 (2019) 12996–13005.

[40] D. Neagu, T.-S. Oh, D.N. Miller, H. Ménard, S.M. Bukhari, S.R. Gamble, R.J. Gorte, J.M. Vohs, J.T. Irvine, Nano-socketed nickel particles with enhanced coking resistance grown in situ by redox exsolution, Nat. Commun. 6 (2015) 8120.

[41] G. Panzner, W. Diekmann, The bonding state of carbon segregated to α-iron surfaces and on iron carbide surfaces studied by electron spectroscopy, Surf. Sci. 160 (1985) 253–270.

[42] J.P. Perdew, K. Burke, M. Ernzerhof, Generalized gradient approximation made simple, Phys. Rev. Lett. 77 (1996) 3865.

[43] J. Peri, Infrared studies of Ni held at low concentrations on alumina supports, J. Catal. 86 (1984) 84–94.

[44] L. Qi, M. Babucci, Y. Zhang, A. Lund, L. Liu, J. Li, Y. Chen, A.S. Hoffman, S.R. Bare, Y. Han, Propane dehydrogenation catalyzed by isolated Pt atoms in ≡ SiOZn–OH nests in dealuminated zeolite Beta, J. Am. Chem. Soc. 143 (2021) 21364–21378.

[45] M. Saidi, M. Safaripour, Pure hydrogen and propylene coproduction in catalytic membrane reactor-assisted propane dehydrogenation, Chem. Eng. Technol. 43 (2020) 1402–1415.

[46] J.J. Sattler, J. Ruiz-Martinez, E. Santillan-Jimenez, B.M. Weckhuysen, Catalytic dehydrogenation of light alkanes on metals and metal oxides, Chem. Rev. 114 (2014) 10613–10653.

[47] M. Shahid, S. Sankarasubramanian, C. He, V.K. Ramani, S. Basu, Ex-solution kinetics of nickel-ceria–doped strontium titanate perovskites, Ionics 27 (2021) 2527–2536.

[48] N. Shi, Y. Xue, Y. Xie, Y. Yang, D. Huan, Y. Pan, R. Peng, C. Xia, Z. Zhan, Y. Lu, Co-generation of electricity and olefin via proton conducting fuel cells using $(Pr_{0.3}Sr_{0.7})_{0.9}Ni_{0.1}Ti_{0.9}O_3$ catalyst layers, Appl. Catal. B: Environ. 272 (2020) 118973.

[49] Y. Sun, J. Li, Y. Zeng, B.S. Amirkhiz, M. Wang, Y. Behnamian, J. Luo, A-site deficient perovskite: the parent for in situ exsolution of highly active, regenerable nano-particles as SOFC anodes, J. Mater. Chem. A 3 (2015) 11048–11056.

[50] Y.-F. Sun, X.-W. Zhou, Y. Zeng, B.S. Amirkhiz, M.-N. Wang, L.-Z. Zhang, B. Hua, J. Li, J.-H. Li, J.-L. Luo, An ingenious Ni/Ce co-doped titanate based perovskite as a coking-tolerant anode material for direct hydrocarbon solid oxide fuel cells, J. Mater. Chem. A 3 (2015) 22830–22838.

[51] P. Tan, Active phase, catalytic activity, and induction period of Fe/zeolite material in nonoxidative aromatization of methane, J. Catal. 338 (2016) 21–29.

[52] R.P. Vasquez, SrTiO$_3$ by XPS, Surf. Sci. Spectra 1 (1992) 129–135.

[53] W. Wang, C. Su, R. Ran, B. Zhao, Z. Shao, M. O. Tade, S. Liu, Nickel-based anode with water storage capability to mitigate carbon deposition for direct ethanol solid oxide fuel cells, ChemSusChem 7 (2014) 1719–1728.

[54] X. Wang, K. Wei, J. Kang, S. Shen, R.A. Budiman, X. Ou, F. Zhou, Y. Ling, Experimental and numerical studies of a bifunctional proton conducting anode of ceria-based SOFCs free from internal shorting and carbon deposition, Electrochim. Acta 264 (2018) 109–118.

[55] L.-C. Wang, Y. Zhang, J. Xu, W. Diao, S. Karakalos, B. Liu, X. Song, W. Wu, T. He, D. Ding, Non-oxidative dehydrogenation of ethane to ethylene over ZSM-5 zeolite supported iron catalysts, Appl. Catal. B: Environ. 256 (2019) 117816.

[56] B.M. Weckhuysen, M.P. Rosynek, J.H. Lunsford, Characterization of surface carbon formed during the conversion of methane to benzene over Mo/H-ZSM-5 catalysts, Catal. Lett. 52 (1998) 31–36.

[57] A. Wiltner, C. Linsmeier, Formation of endothermic carbides on iron and nickel, Phys. Status Solidi (a) 201 (2004) 881–887.

[58] W. Wu, H. Hu, D. Ding, Low-temperature ethylene production for indirect electrification in chemical production, Cell Rep. Phys. Sci. 2 (2021) 100405.

[59] W. Wu, L.-C. Wang, H. Hu, W. Bian, J.Y. Gomez, C.J. Orme, H. Ding, Y. Dong, T. He, J. Li, Electrochemically Engineered, Highly Energy-Efficient Conversion of Ethane to Ethylene and Hydrogen below 550 °C in a Protonic Ceramic Electrochemical Cell, ACS Catal. 11 (2021) 12194–12202.

[60] L. Yang, S. Wang, K. Blinn, M. Liu, Z. Liu, Z. Cheng, M. Liu, Enhanced sulfur and coking tolerance of a mixed ion conductor for SOFCs: $BaZr_{0.1}Ce_{0.7}Y_{0.2-x}Yb_xO_{3-\delta}$, Science 326 (2009) 126–129.

[61] L. Zeng, K. Cheng, F. Sun, Q. Fan, L. Li, Q. Zhang, Y. Wei, W. Zhou, J. Kang, Q. Zhang, Stable anchoring of single rhodium atoms by indium in zeolite alkane dehydrogenation catalysts, Science 383 (2024) 998–1004.

[62] R. Zhang, Y. Meng, L.-C. Wang, M. Wang, W. Wu, W. Wu, D. Ding, Boosting the performances of protonic solid oxide fuel cells for co-production of propylene and electricity from propane by integrating thermo- and electro- catalysis, Fuel 357 (2024).

[63] Z. Ziaka, R. Minet, T. Tsotsis, A high temperature catalytic membrane reactor for propane dehydrogenation, J. Membr. Sci. 77 (1993) 221–232.